Effects of Hydraulic Fracturing Fluid Chemistry on Shale Matrix Permeability

Abdulgader Alalli*[1], Qingyun Li[1,2], Adam Jew[2], Arjun Kohli[1,2], John Bargar[2], Mark Zoback[1], Anthony Kovscek[1]; 1. School of Earth, Energy & Environmental Sciences, Stanford University, *2*. SLAC National Accelerator Laboratory.

Abstract

Shale reservoirs are characterized with having an ultra-low permeability, such that in order to produce these reservoirs economically, hydraulic fractures are created and flushed with large volumes of fracture fluid chemicals to help aid with well production. In this study, we aim to understand how fracture fluid affects the permeability of the shale matrix from either porosity enhancement or mineral precipitation due to the shale's mineral composition. We conducted laboratory permeability measurements on intact horizontal shale microcore samples from both Eagle Ford and Marcellus reservoirs before and after reaction with a dissolution-favored synthetic fracturing fluid (pH = 2). Shale reactions with fracture fluid were performed inside a batch reactor set at 80°C and 77bar for 6 days, with added $BaCl_2$ and Na_2SO_4 salts in place of barite-rich drilling mud to promote barite precipitation. Our results show a permeability reduction for the clay-rich Marcellus, while permeability was significantly enhanced for the Eagle Ford sample. Additionally, SEM image observations and energy diffusive spectroscopy (EDS) provided supporting evidence for mineral composition changes post fracture fluid reaction. The occurrence of barite precipitation in the Marcellus sample and accumulation inside the limited microcracks, resulted in occlusion of the main transport flow paths and a reduction in permeability. As for the Eagle Ford sample, even though barite precipitation also occurs in the microcracks, the rate of carbonate dissolution is far greater, creating a large amount of secondary porosity and an order of magnitude increase in permeability. By demonstrating the complex interactions of fracture fluid chemistry with the shale matrix and its effect on permeability, we suggest that fracture fluid recipes could be tailored specifically to the mineral composition for each shale reservoir in order to enhance production of stimulated shale volumes.

Introduction

During hydraulic fracturing, large volumes of fracture fluids are flushed into the reservoir to help enhance permeability and well production. Combined with the technological advancement of hydraulic stimulation along horizontal wells, unconventional shale reservoirs, characterized with having an ultra-low intrinsic permeability, are now able to be extracted and produced economically. In spite of this progression, unconventional shale reservoir production remains highly inefficient, with industry reported recovery factors of around 25% for gas (Rassenfoss, 2018) and rapid rate declines a few years after initial production (Valko and Lee, 2010), suggesting that a large portion of the resource is still left trapped, as adsorbed gas, inside the nanopores of the shale matrix (Ambrose et al., 2010). Although shale mineral composition is considered to be a main factor controlling shale permeability (Ismail and Zoback, 2016; Chalmers et al., 2012), there is a shortage of experimental work looking at fracture fluid chemical reactions on shale matrix permeability of intact cores with varying mineral composition. In this study, our

goal is to understand how fracture fluid affects the permeability of the shale matrix from either porosity enhancement or mineral precipitation due to the shale's mineral composition. The main chemical reaction we focused on is barite scale formation from drilling mud, which can reduce permeability and hinder well production (Kan and Tomson, 2012). Deconvolving the factors that influence permeability (fluid vs. chemical effects) is crucial for optimizing production strategies.

Sample Description

      Two types of shale samples are presented in this paper, a clay-rich Marcellus shale and a carbonate-rich Eagle Ford shale. The Marcellus shale was retrieved from Eastern Gas Shales Project well PA-5 in Lawrence County, PA at a depth of 4130ft (Carter et al. 2011), while the Eagle Ford shale was provided from Southwest Texas at a depth of 11000ft. Both samples are horizontal cores, drilled parallel to the bedding planes, and measured having a 25mm diameter and 15mm length prior to mini-coring (to be discussed further in permeability experimental setup).

Table 1. Shale mineral compositions from XRD by weight percentage prior to fracture fluid reaction.

Sample	Depth (ft)	Carbonates	QFP	Clays	Pyrite
Eagle Ford[*]	11000	53	22	22	3
Marcellus[*]	4130	7	41	41	11

    *Both samples are horizontal cores drilled parallel to the bedding planes.

Methods

Permeability Experimental Setup:

      Permeability measurements follow the same experimental setup used by (Heller et al., 2014; Al Ismail et al., 2014). Samples were loaded inside a hydrostatic pressure vessel core holder connected to an isco 100DX syringe pump for confining pressure. A Heise DXD pressure transducer was attached to the syringe pump to measure confining pressure within ±0.1% accuracy. While a Quizix Qx-6000 dual piston pump was used to control pore pressure of both upstream and downstream lines via floating distribution plugs and connected to an Argon gas tank. We selected argon gas for all permeability measurements since it is non-adsorbing and has a similar molecular diameter to methane. Both systems were placed inside a thermal isolation box with a heating fan, as shown in Figure 1 (left). Temperature was set to $38^{\circ}C$ and stability was maintained with thermocouples set along both pore pressure and confining pressure lines and a controller system implemented in LabView to keep temperature constant.

      Samples were cored down from 25mm diameter core plugs to 10mm diameter microcores due to the size limitation of our batch reactor (sample max diameter: 24mm). We designed a PTFE (Teflon) annulus adapter (dimensions OD/ID: 24mm/11mm) and epoxied the microcores into the annulus with heat- and chemical-resistant epoxy (No. EP42HT-2, Master Bond® Inc.) in order to fit into both the batch reactor and core holder, as seen on Figure 1 (right). We chose Teflon since it is chemically resistive to the fracture fluid and compressible.
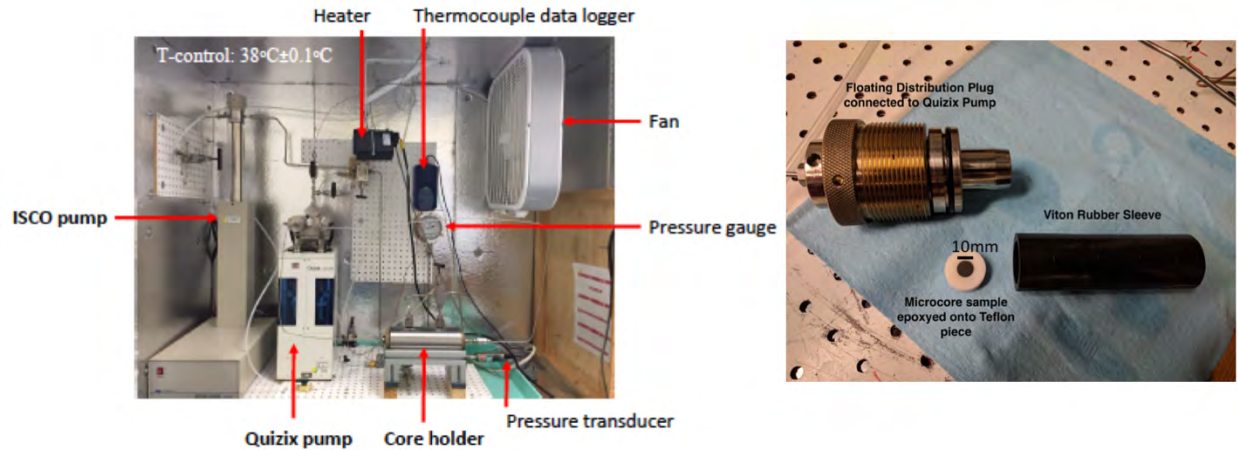
Figure 1: Experimental setup set inside temperature control box for hydrostatic permeability measurements (left) (Image from: Al Ismail and Zoback, 2016). Sample microcore epoxied onto PTFE annulus adapter to fit into core holder and batch reactor (right).

Due to the low permeability of shales, we chose the pressure pulse decay method developed by Brace et al. (1968) but with a modified constant upstream pressure to compensate for any gas leakage along the upstream volume (Zoback and Byerlee, 1975). An example of the downstream pressure recorded during a pulse permeability is shown in Figure 2. Then by taking the natural log of the pressure difference between upstream and downstream reservoirs ln(ΔP), we get a linear trend (α) of the natural log of the pressure decay difference when plotted over time, and fitted by the following equation (Brace et. al, 1968)

$$\Delta P(t) = \Delta P_0 e^{-\alpha t} \qquad\qquad\qquad\qquad\qquad\qquad\qquad\qquad\qquad \text{Eq.1}$$

$$\alpha = \frac{kA}{\beta V_{dn} L \mu} \qquad\qquad\qquad\qquad\qquad\qquad\qquad\qquad\qquad\qquad \text{Eq.2}$$

Where ΔP_0 is the pressure difference at t=0, β is the gas compressibility, μ is the gas dynamic viscosity, L is the sample length, A is the sample cross sectional area, V_{dn} is the downstream reservoir volume, and k is the sample permeability, for which we solve for.
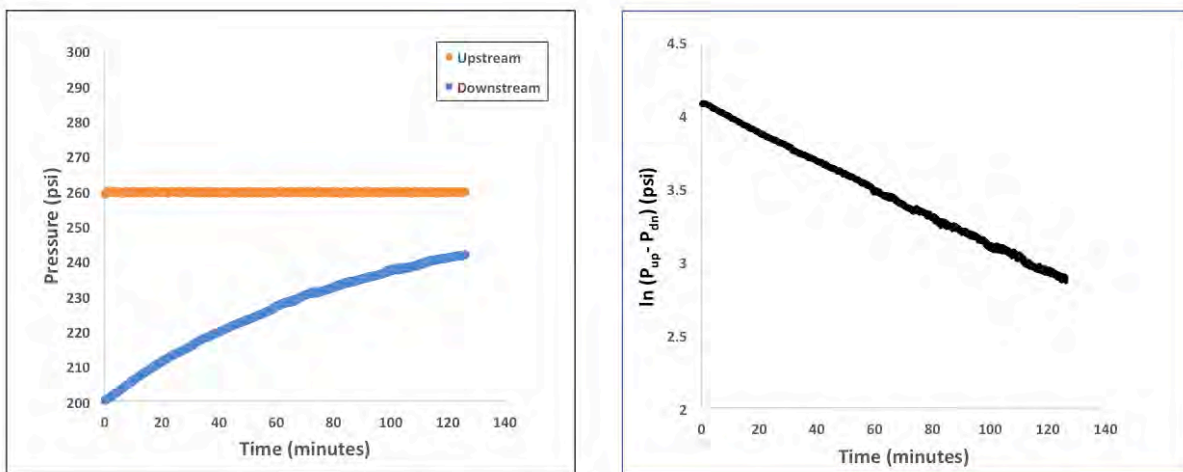

Figure 2: Pulse permeability example showing both upstream and downstream recorded pressure curves (left) and the natural logarithmic decay of the pressure difference between both upstream and downstream reservoirs (right).

The experimental protocol involves three parts. For each microcore, we measure pre-reaction permeability, perform synthetic fracture fluid reaction in the batch reactor, and finally measure post-reaction permeability. We performed 4 permeability measurements on each microcore, where the first 3 measurements were used to calculate the intrinsic permeability, while the last measurement was set to relative reservoir production conditions. We repeat the same procedure for the same sample post-reaction, for a total of 8 permeability measurements per sample, as shown in Figure 3.
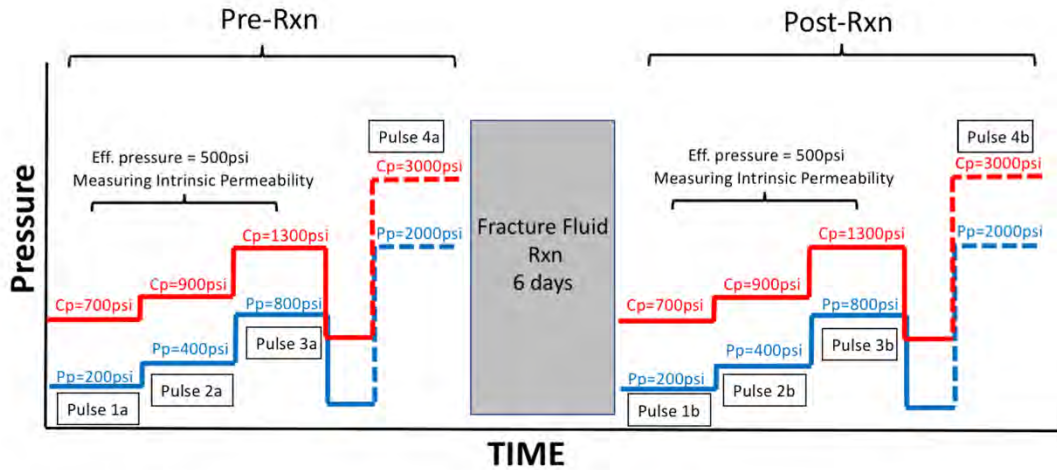

Figure 3: Scheduled experimental procedure showing the incremental confining and pore pressure steps for each sample during pre- and post-reaction, while fracture fluid reactions in the batch reactor are scheduled in between. Pulse permeability measurements #1-3 are conducted with increasing pore pressure and a constant effective pressure=500psi to measure intrinsic permeability, while permeability measurement #4 is set at an effective pressure=1000psi, similar to relative reservoir production conditions.

Fracture Fluid Reaction Setup:

A synthetic fracture fluid solution was prepared following the same recipe used by Jew et al. (2017), which is based on National Energy Technology Laboratory's (NETL) fracture fluid composition used for Frac jobs done in Greene County, PA Marcellus well E (Hammack et al., 2014). Table 1 lists the ingredients used in the fracture fluid.

Table 1. Synthetic fracture fluid chemistry. Based on NETL's Greene County, PA, Well E.

Ingredient	Purpose	Percentage of Ingredient (by mass)
Water	Base Fluid	99.783%
Ethylene Glycol	Scale Inhibitor, Iron Control, Breaker	0.021%
Kerosene	Friction Reducer	0.024%
Guar Gum	Dry Gellant	0.029%
2-Ethyl hexanol	Corrosion Inhibitor for Acid	0.0005%
Glycol ether	Corrosion Inhibitor for Acid	0.0002%
Polyethylene glycol	Biocide	0.020%
Hydrochloric acid	Acid	0.122%

In addition to the dissolution favorable (pH = 2) fracture fluid solution, 2 mM $BaCl_2$ and 0.06 mM Na_2SO_4 (SI_{barite} = 1.3) was added to the solution to act in place of barite found in drilling mud, where the added salt will promote barite scale formation in the shale microcore.

The samples are then placed into a batch reactor setup following the same experimental procedure outlined by Li et al., 2018. The batch reactor was set at $80°C$ and pressurized with N_2 at 77bar for a duration of 6 days. After reaction, samples were removed from fracture fluid and oven dried at $45°C$ until sample weight has stabilized.

Scanning Electron Microscopy with Energy Dispersive Spectroscopy
        In preparation for Imaging, microcores were progressively smoothed using sand paper (600 grit, followed by 1500 grit), then polished using diamond grit (6μm, followed by 1μm). The samples were attached to aluminum mounts with a fine coating of fast drying silver paint (Pelco® Conductive Silver Paint) on the base and along the sides of the sample to improve conductivity. Finally, samples were sputter coated with gold to reduce charging problems.

        High-resolution SEM images were collected on an FEI Magellan 400 XHR, linked with a Bruker Quantax XFlash energy dispersive spectroscopy (EDS). Images were acquired at fiducial points along the microcore shale surface that we could easily identify pre- and post-reaction to the fracture fluid and allows us to see any alteration occurring as a result of either mineral dissolution or precipitation within the shale matrix. All SEM images acquired are backscattered electron images using a concentric backscatter detector with inner a-ring attached (CBS-a), to provide the best elemental contrast and remove any topographical discrepancy across the sample surface. All EDS analysis was collected using the following settings: beam voltage 15kV, beam current 13nA, magnification of 150x-200x in order to include as much surface area into the analysis.

        From the acquired EDS qualitative elemental maps, object classification images were produced using Quantax Esprit 2.1 software. The object classification images are based on a combination of both principal component analysis and cluster analysis of neighboring points from EDS data. We classify the objects into the following phases: (1) Silicate- or Clay-rich Matrix (green), (2) Organic Matter (blue), (3) Clay (pink), (4) Carbonate (cyan), (5) Pyrite (red), (6) Silicates (magenta), (7) Barite (yellow), and the remainder black clusters represent pore space.

Results and Analysis

Permeability Measurements
        In Figure 4, we show results for both pre- and post-reaction permeability measurements done on the Marcellus (left) and Eagle Ford (right) microcores. For the Marcellus microcore, a decrease in measured permeability is observed for post-reaction measurements (0.040, 0.027, 0.022, 0.015μdarcy) compared to pre-reaction measurements (0.049, 0.032, 0.025, 0.019 μdarcy) at increasing pore pressures (200, 400, 800, 2000 psi), respectively. As for the Eagle Ford microcore, the opposite trend is noticed, showing a large increase in measured permeability for post-reaction measurements (3.361, 3.059, 2.799, 0.767μdarcy) compared to pre-reaction measurements (0.431, 0.342, 0.254, 0.088μdarcy) at same increasing pore pressure steps.
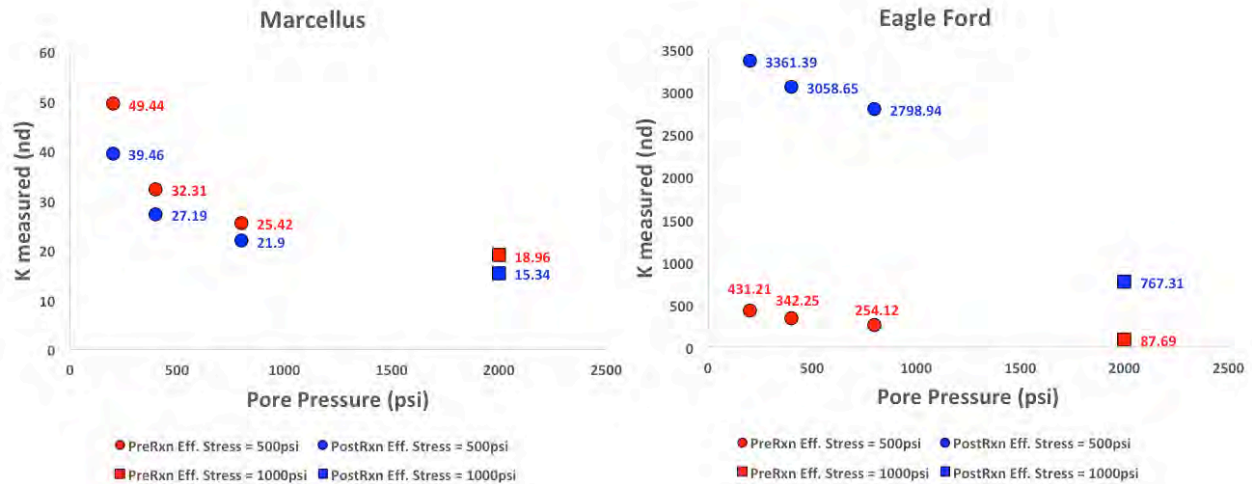
Figure 4: Measured Permeability for pre- and post-reaction Marcellus (left) and Eagle Ford (right) samples. Pulse permeability measurements were acquired at incrementally increasing pore pressures (200psi, 400psi, 800psi) while maintaining an effective pressure=500psi in order to calculate the intrinsic permeability from Klinkenberg analysis. An additional permeability measurement was collected at pore pressure=2000psi and effective pressure=1000psi to replicate relative reservoir production conditions.

We extend our findings to compute the intrinsic permeability of each sample using Klinkenberg analysis. Following Klinkenberg's equation, a linear fit is observed between inverse pore pressure and measured permeability (1941), such that intrinsic permeability is equal to the y-intercept.

$$K_{measured} = K_\infty \left(1 + \frac{K_b}{Pp}\right) \qquad\qquad\qquad Eq.3$$

Utilizing the first 3 pulse measurements set at increasing pore pressures 200psi, 400psi, 800psi, while maintaining a constant effective pressure at 500psi, we calculate the intrinsic permeability (K_∞) for each sample as shown in Figure 5. We observe the same trend as seen on the measured permeability results for each sample, where a minor decrease in intrinsic permeability going from 0.017µdarcy to 0.015µdarcy for the Marcellus microcore. While an increase, by an order of magnitude, in the Eagle Ford intrinsic permeability is observed going from 0.209µdarcy to 2.648µdarcy. This highlights a 6.5% reduction in Marcellus permeability and a 1000% increase in Eagle Ford permeability post-reaction with fracture fluid.
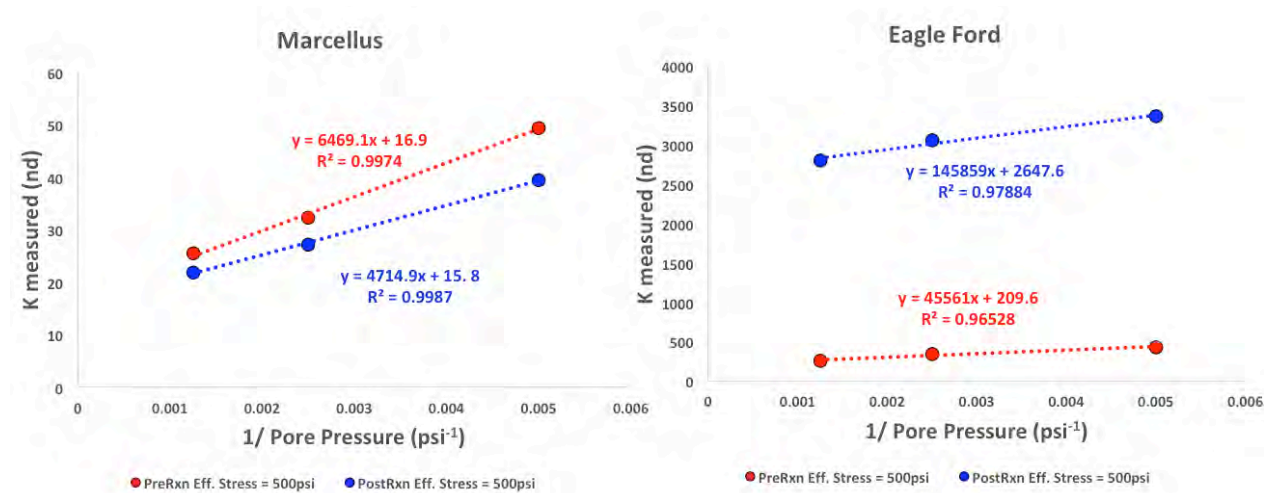
Figure 5: Klinkenberg analysis for pre- and post-reaction Marcellus (left) and Eagle Ford (right) samples done for varying pore pressures at constant effect pressure=500psi. From the fitted trend line, the y-intercept is the intrinsic permeability (K_∞). We show the intrinsic permeability of the Marcellus sample reduced post-reaction to fracture fluid, while the Eagle Ford shows an order of magnitude increase in intrinsic permeability post-reaction.

Imaging and Elemental Analysis

In figures 6 and 7, we showcase a series of sequential images highlighting the changes pre- (top row) and post-reaction (bottom row) with the fracture fluid. A backscattered SEM image with CBS-a detector (left) shows the textural changes along the shale matrix and microcracks, while the object classification image shows the mineralogy identified from clusters analysis of EDS data (middle), and the final column (right) combines both images to get a composite image. Since barite precipitation was observed from experiments done by Li et al. (2018) for the same sample set, we added barite into the object classification using the acquired barium and sulfur elemental maps.

For the Marcellus (Figure 6) pre-reaction sample (top row), we note a clay-rich matrix (green), silicate minerals (magenta) and pyrite (red) dispersed across the matrix, and a large microcrack filled with organic matter (blue). Comparing it to the post-reaction images (bottom row), no secondary porosity generation is evident across the backscattered (bottom left), whereas the microcracks are filled with a high contrasting mineral. From the object classification image (bottom middle), we identify the bright mineral as barite (yellow) in the form of precipitates dispersed across the matrix but predominantly deposited into the microcracks and occluding them.

As for the Eagle Ford (Figure 7) pre-reaction sample (top row), we note a carbonate-rich matrix (green), clay platelets (pink), carbonate grains aggregated together (cyan), organic matter (blue), pyrite (red) dispersed across the matrix, and a few large microcracks running parallel to bedding. Looking now at the post-reaction images (bottom row), the microcracks are filled with barite precipitates as shown on the object classification image (bottom middle), but also most carbonate grains have been dissolved by the fracture fluid, resulting in the generation of secondary porosity across the shale matrix.
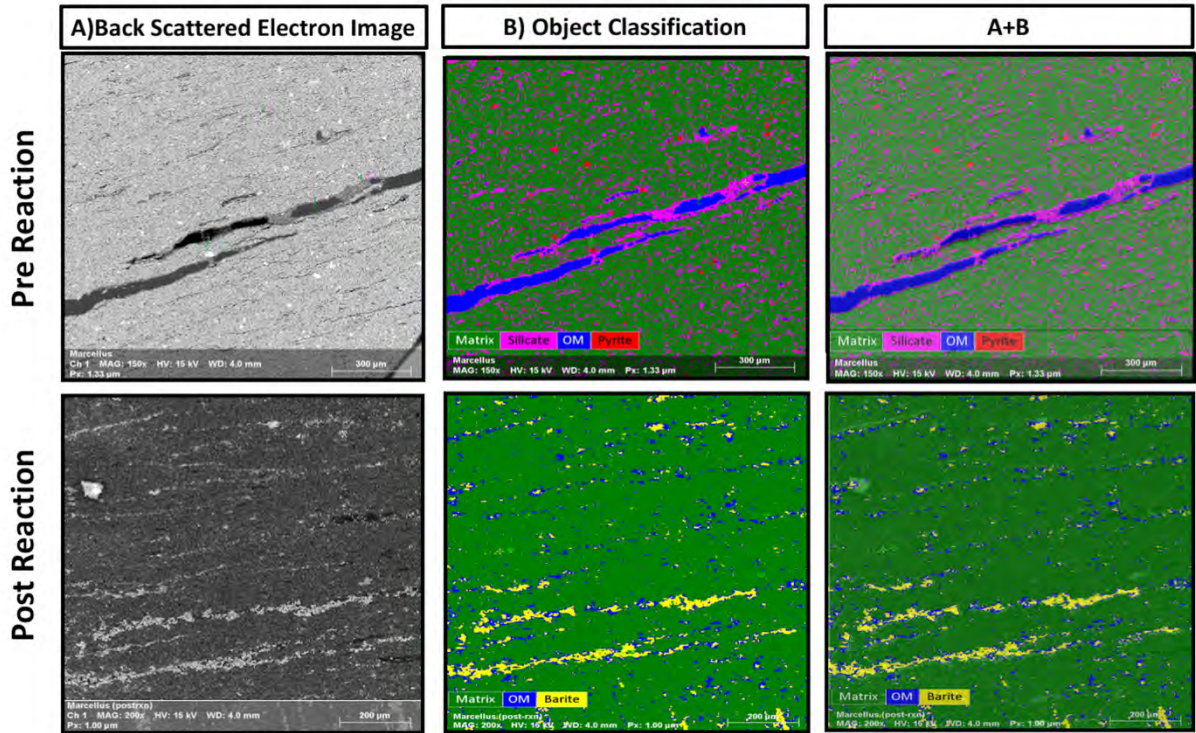
Figure 6: SEM and EDS images for Marcellus pre- (top row) and post-reaction (bottom row) to fracture fluid. Backscattered electron (CBS-a) images emphasize the shale texture and microcracks across the sample (right). The middle column shows object classification derived from EDS cluster analysis. From the overlay of both images (left), we note the barite precipitates deposited into the microcracks as a result of the fracture fluid reaction.
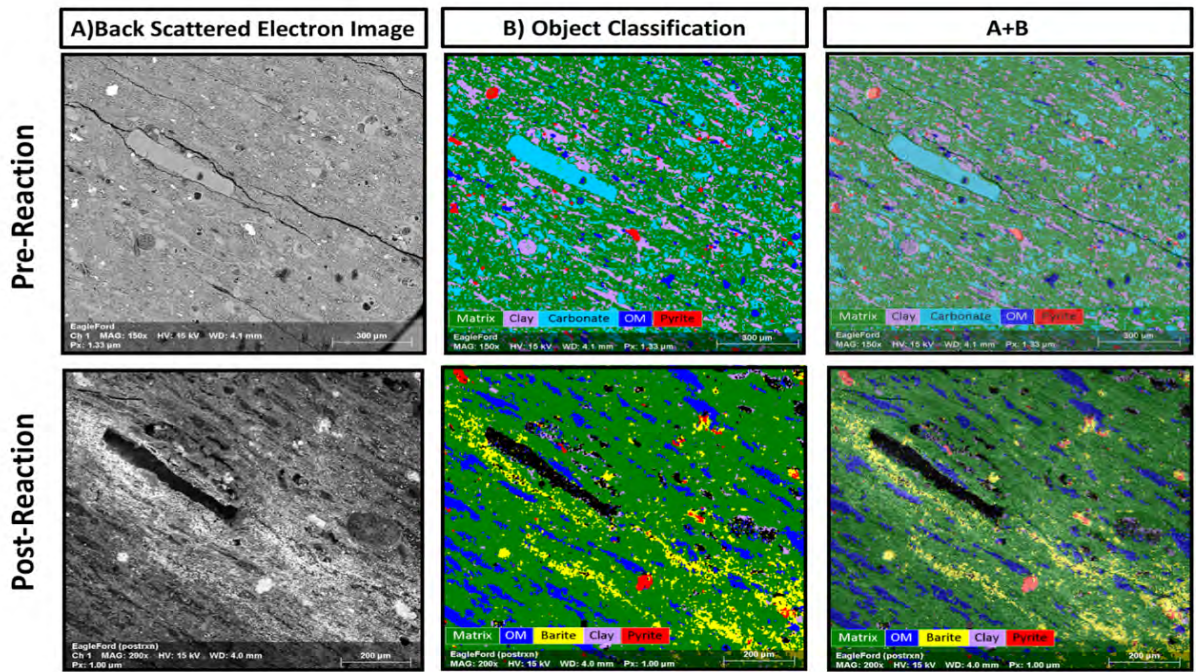

Figure 7: SEM and EDS images for Eagle Ford pre- (top row) and post-reaction (bottom row) to fracture fluid. Backscattered electron (CBS-a) images emphasize the shale texture and microcracks across the sample (left). The middle column shows object classification derived from EDS cluster analysis. From the overlay of both images (right), we note the barite precipitates deposited into the microcracks, but also exhibit prevalent secondary porosity generation (black regions) due to the dissolution of carbonates (cyan) from the fracture fluid reaction.

Discussion

Results from our permeability measurements show that shale mineral composition is a main factor to consider when reacting with the fracture fluid and subsequently affecting post-reaction permeability. In the case of the Marcellus microcore, the clay-rich sample exhibits a permeability reduction post-reaction to the fracture fluid. This reduction can be explained by the presence of barite precipitates, as seen in the EDS object classification images, being deposited into the microcracks and blocking the main transport pathways for flow across the sample. Even though the fracture fluid is a dissolution-favored solution, there is no observable secondary porosity generated in the Marcellus microcore. Contrasting this to the Eagle Ford microcore, the carbonate-rich sample measured an order of magnitude increase in intrinsic permeability, predominantly from calcite dissolution (as seen from EDS object classification), leading to the creation of secondary porosity across the whole microcore surface in contact with the solution. Even though barite precipitates were observed and deposited into microcracks, the rate of mineral dissolution was far greater than barite precipitation. Hence why the kinetics of mineral dissolution to precipitation is of outmost importance when designing fracture fluid recipes that need to take into account the shale matrix mineral composition.

Conclusions

Fracture fluids flushed during hydraulic fracturing jobs are used to enhance permeability and aid production of unconventional shale reservoirs. Our results emphasize the importance of shale matrix mineral composition can have on permeability during fracture fluid reaction. We show that for a dissolution-favored fracture fluid solution, permeability enhanced in the Eagle Ford sample, while it reduced in the Marcellus sample. Further investigation using SEM imaging and EDS analysis shows barite precipitates accumulating inside the microcracks in both samples, but the rate of calcite dissolution was far greater for the carbonate-rich Eagle Ford sample than in the clay-rich Marcellus. Consequently, tailoring specific fracturing fluid recipes that would take into account shale mineralogical composition can lead to enhanced permeability of stimulated shale volumes by reducing the formation of scale precipitates and increasing shale matrix pore accessibility.

References

Al Ismail, M. I. and M. D. Zoback (2016). "Effects of Rock Mineralogy and Pore Structure on Stress-Dependent Permeability of Shale Samples." Phil. Trans. R. Soc. A **374**(2078): 20150428.

Al Ismail, M., Reece, J. S., Hol, S., & Zoback, M. (2014). "The Effect of CO2 Adsorption on Permeability Anisotropy in the Eagle Ford Shale." Unconventional Resources Technology Conference (URTEC).

Ambrose, R. J., Hartman, R. C., Diaz Campos, M., Akkutlu, I. Y., & Sondergeld, C. (2010). New pore-scale considerations for shale gas in place calculations. In SPE Unconventional Gas Conference. Society of Petroleum Engineers.

Brace, W. F., J. B. Walsh, and W. T. Frangos, (1968). "Permeability of granite under high pressure." Journal of Geophysical Research **73**: 2225–2236

Carter, K. M., J. A. Harper, K. W. Schmid and J. Kostelnik (2011). "Unconventional Natural Gas Resources in Pennsylvania: The Backstory of the Modern Marcellus Shale Play." Environmental Geosciences **18**(4): 217-257.

Chalmers, G. R., Ross, D. J., & Bustin, R. M. (2012). "Geological controls on matrix permeability of Devonian Gas Shales in the Horn River and Liard basins, northeastern British Columbia, Canada". International Journal of Coal Geology 103: 120-131.

Hammack, R., W. Harbert, S. Sharma, B. Stewart, R. Capo and A. Wall (2014). "An Evaluation of Fracture Growth and Gas/Fluid Migration as Horizontal Marcellus Shale Gas Wells are Hydraulically Fractured in Greene County, Pennsylvania." National Energy Technology Laboratory: NETL-TRS-3-2014, 76pp. https://www. netl. doe. gov/File% 20Library/Research/onsite% 20research/publications/NETL-TRS-3-2014_Greene-County-Site_20140915_1_1. pdf.

Heller, R., J. Vermylen and M. D. Zoback (2014). "Experimental Investigation of Matrix Permeability of Gas Shales." AAPG bulletin **98**(5): 975-995.

Jew, A. D., M. K. Dustin, A. L. Harrison, C. M. Joe-Wong, D. L. Thomas, K. Maher, G. E. Brown Jr and J. R. Bargar (2017). "Impact of Organics and Carbonates on the Oxidation and Precipitation of Iron During Hydraulic Fracturing of Shale." Energy & Fuels **31**(4): 3643-3658.

Kan, A. and M. Tomson (2012). "Scale Prediction for Oil and Gas Production." Spe Journal **17**(02): 362-378.

Klinkenberg, L. J., (1941). "The permeability of porous media to liquids and gases." Drilling and production practice: American Petroleum Institute: 200–213.

Li, Q., A. Jew, A. Kiss, A. Kohli, A. Alalli, A. Kovscek, M. D. Zoback, D. Cercone, K. Maher, G. Brown, J. R. Bargar (2018). "Imaging Pyrite Oxidation and Barite Precipitation in Gas and Oil Shales". Unconventional Resources Technology Conference (URTEC), Houston, Texas, USA.

Rassenfoss, S., (2018). "Building wells with an eye for the future". Journal of Petroleum Technology (JPT) **70**(4)

Valko, P. P., and Lee, W. J. (2010). "A Better Way To Forecast Production From Unconventional Gas Wells". Society of Petroleum Engineers (SPE) doi:10.2118/134231-MS

Zoback, M. D., and J. D. Byerlee, (1975). "Permeability and Effective Stress." AAPG Bulletin **59**: 154–158.